

Spatiotemporal analysis for detection of pre-symptomatic shape changes in neurodegenerative diseases: applied to GENFI study

Claire Cury^{a,b,c}, Stanley Durrleman^e, David Cash^{a,b}, Marco Lorenzi^{a,f}, Jennifer M Nicholas^{b,g}, Martina Bocchetta^b, John C. van Swieten^h, Barbara Borroniⁱ, Daniela Galimberti^j, Mario Masellis^k, Maria Carmela Tartaglia^l, James B Rowe^m, Caroline Graff^{n,o}, Fabrizio Tagliavini^p, Giovanni B. Frisoni^q, Robert Laforce Jr^r, Elizabeth Finger^s, Alexandre de Mendonça^t, Sandro Sorbi^{u,v}, Sébastien Ourselin^{a,b,d}, Jonathan D. Rohrer^b, Marc Modat^{a,b,d}, on behalf of the Genetic FTD Initiative, GENFI.¹

^aDepartment of Medical Physics and Biomedical Engineering, University College London

^bDementia Research Centre, Institute of Neurology, University College London, London WC1N 3BG, United Kingdom

^cVISAGES team, Inria Bretagne atlantique, Rennes, France

^dSchool of Biomedical Engineering and Imaging Sciences, King's College London, United Kingdom

^eInria Aramis project-team Centre Paris-Rocquencourt, Inserm U 1127, CNRS UMR 7225, Sorbonne Universités, UPMC Univ Paris 06 UMR S 1127, Institut du Cerveau et de la Moelle épinière, ICM, F-75013, Paris, France

^fEpione team, Inria Sophia Antipolis, Sophia Antipolis, France

^gDepartment of Medical Statistics, London School of Hygiene & Tropical Medicine, London, United Kingdom

^hErasmus Medical Center, Rotterdam, Netherlands

ⁱUniversity of Brescia

^jDept. of Pathophysiology and Transplantation, "Dino Ferrari" Center, University of Milan, Fondazione C Granda, IRCCS Ospedale Maggiore Policlinico, Milan, Italy

^kCognitive Neurology Research Unit, Sunnybrook Health Sciences Centre; Hurvitz Brain Sciences Research Program, Sunnybrook Research Institute; Department of Medicine, University of Toronto

^lTanz Centre for Research in Neurodegenerative Diseases, University of Toronto

^mUniversity of Cambridge

ⁿKarolinska Institutet, Stockholm, Sweden, Karolinska Institutet, Department NVS, Center for Alzheimer Research, Division of Neurogeriatrics, Sweden

^oDepartment of Geriatric Medicine, Karolinska University Hospital, Stockholm, Sweden

^pIstituto Neurologico Carlo Besta, Milan, Italy

^qIRCCS San Giovanni di Dio Fatebenefratelli Brescia, Italy

^rUniversité Laval, Québec, Canada

^sUniversity of Western Ontario, Ontario, Canada

^tFaculdade de Medicina, Universidade de Lisboa, Portugal

^uDepartment of Neurosciences, Psychology, Drug Research and Child Health (NEUROFARBA), University of Florence, Florence, Italy

^vIRCCS Don Gnocchi, Firenze, Italy

Abstract

Brain atrophy as measured from structural MR images, is one of the primary imaging biomarkers used to track neurodegenerative disease progression. In diseases such as frontotemporal dementia or Alzheimer's disease, atrophy can be observed in key brain

¹List of consortium members in appendix.

structures years before any clinical symptoms are present. Atrophy is most commonly captured as volume change of key structures and the shape changes of these structures are typically not analysed despite being potentially more sensitive than summary volume statistics over the entire structure.

In this paper we propose a spatiotemporal analysis pipeline based Large Diffeomorphic Deformation Metric Mapping (LDDMM) to detect shape changes from volumetric MRI scans. We applied our framework to a cohort of individuals with genetic variants of frontotemporal dementia and healthy controls from the Genetic FTD Initiative (GENFI) study. Our method, take full advantage of the LDDMM framework, and relies on the creation of a population specific average spatiotemporal trajectory of a relevant brain structure of interest, the thalamus in our case. The residuals from each patient data to the average spatiotemporal trajectory are then clustered and studied to assess when presymptomatic mutation carriers differ from healthy control subjects.

We found statistical differences in shape in the anterior region of the thalamus at least five years before the mutation carrier subjects develop any clinical symptoms. This region of the thalamus has been shown to be predominantly connected to the frontal lobe, consistent with the pattern of cortical atrophy seen in the disease.

Keywords: Shape, thalamus, spatiotemporal geodesic regression, parallel transport

1. Introduction

2 Neurodegenerative diseases such as frontotemporal dementia (FTD) present with pro-
3 gressive symptoms of behavioural and cognitive dysfunction. These changes follow many
4 years of a clinically silent phase in the disease, where abnormal protein pathology slowly
5 accumulates within the brain, leading to neurodegenerative processes that ultimately
6 result in loss of function. Reliably identifying presymptomatic changes in individuals
7 could lead to intervention with therapies that could slow, or even halt, the onset of these
8 diseases. However, finding a cohort of presymptomatic individuals guaranteed to develop
9 a form of dementia can be challenging. One common strategy is to investigate people
10 who are at-risk for rare autosomal dominant forms of dementia. Half of these individuals
11 are carriers of the mutation, allowing for comparisons between carriers and non-carriers
12 at various stages within the disease process. In the case of genetic FTD, roughly one
13 third of all cases are caused by autosomal dominant mutations, primarily in three genes:
14 chromosome 9 open reading frame 72 (*C9orf72*), progranulin (*GRN*), and microtubule
15 associated protein tau (*MAPT*) [1]. As the name would suggest, in all mutations, there
16 is early involvement of both the frontal and temporal lobes, as well as the insula where
17 differences can be observed as early as ten years before estimated age of expected symp-
18 tom onset, as shown in Rohrer *et al.* [2]. However, there are additional structures, such as
19 the thalamus, which also appear to be implicated to some degree early on in the disease
20 process [3]. In many forms of FTD, clinical presentations suggest a left/right asymmetry
21 in terms of which hemisphere is more affected, and this is often supported by evidence
22 of increased atrophy within the affected hemisphere [4]. However, the affected side is

23 not consistent across all cases, and in some cases, there is no evidence of an asymmetry.
24 As this asymmetry is likely to start early in the disease process, it must be taken into
25 account when looking to detect early changes with any sensitivity.

26 One biomarker that shows promise during the presymptomatic phase is measurement
27 of atrophy derived from structural magnetic resonance imaging (MRI) [5, 2, 6] Volumes
28 summarizing change within a region of interest (ROI) tend to be more sensitive to early
29 change than voxelwise approaches, but they do not provide any spatial localisation as
30 to where the atrophy is occurring within the ROI. Conversely, voxelwise analysis can
31 provide better spatial localisation, but the mass univariate nature of the analysis requires
32 correction for multiple comparisons to control for false positive findings, which often
33 results in reduced sensitivity. As loss of brain volume will imply a change in the shape of
34 the structure, a third option is to perform the shape analysis over time for a structure of
35 interest. This could provide more spatial information than a single summary measure of
36 volume alone, but does not require the same level of multiple comparisons as a voxelwise
37 analyses. Given the decades long nature of the disease process, it is not yet feasible
38 to measure the complete time course within one individual. Therefore, the pattern
39 of atrophy over the course of the disease must be estimated through spatiotemporal
40 regression models based on large populations of either cross-sectional data or through
41 longitudinal data that covers a smaller segment (i.e. a few years) of the disease process
42 within each individual.

43 There have been numerous approaches to spatiotemporally model trajectories of ageing
44 and dementia. Some methods model this evolution using dense 4D deformation fields
45 to measure change between timepoints. Lorenzi *et al.* [7] modelled the 4D deformation
46 fields within a population to obtain subject-specific measurements of atrophy. An ex-
47 tension of this work discriminated spatiotemporal patterns that could be attributed to
48 natural ageing versus to those that were related to disease [8]. Other groups estab-
49 lish point correspondences between subjects on a surface representation, and then apply
50 mixed effects models at those points [9, 10, 11], providing fixed effects that represent the
51 change across the overall population while allowing individual longitudinal trajectories
52 as random effects. Using more complex representations of surfaces, Durrleman *et al.* [12]
53 proposed a spatiotemporal regression approach to estimate continuous subject-specific
54 trajectories of longitudinal data.

55 In our previous work [13], we defined the shape of the structure of interest as its 3D
56 outline that is rotation and translation invariant. Differences between shapes were quan-
57 tified using the Large Deformation Diffeomorphic Metric Mapping (LDDMM) frame-
58 work [14, 15, 16], producing a smooth and invertible continuum between all possible
59 shapes within the population. The smooth representation of these deformations also
60 acted as low-pass filter, reducing the effects of irregularities and errors in the surface
61 boundaries. Overall, our approach consisted of three main steps. First, using all avail-
62 able data, we compute an average shape spatiotemporal trajectory. Second, for every
63 individual shape we evaluate its distance from the mean trajectory. Last, after spatially
64 normalising all the subject-specific distances to the mean, we run a statistical analysis
65 on the subject-specific residuals to assess when a shape starts diverging from normality.
66 This previous work presented a global spatio-temporal analysis, on one side of the brain,
67 without considering a potential asymmetry of the disease. In this paper, we build on
68 the aforementioned framework, which we altered in two main ways. First, we take into
69 consideration the potential asymmetry of FTD by considering the left and right struc-

70 tures using a common shape representation. Second, we modified our feature extraction
71 method using a clustering approach to ensure we can attribute the recovered differences
72 to substructure of the shape under study, and made a novel local analysis, based on
73 cluster of deformations, taking better advantage of the LDDMM framework.

74 We apply this approach to data from the Genetic FTD Initiative (GENFI), an in-
75 ternational study of autosomal dominant forms of FTD aimed at collecting multimodal
76 neuroimaging, alongside other biomarkers with the objective of obtaining an improved
77 understanding of the changes that are occurring during the presymptomatic phase of
78 the disease. In general, the expected age of onset of clinical symptoms is estimated by
79 using the average age of onset in the family of the subject, allowing to align the different
80 subjects onto a single time axis. We applied our method to a subcortical structure, the
81 thalamus, which has been shown to present volumetric differences before onset in Rohrer
82 *et al.* [2]. We used the expected age to onset to characterise the time progression. In the
83 next section, we will present the different steps of the proposed framework before then
84 further describing the experiment and associated results.

85 **2. Method**

We indicate with $\{(S_i, t_i)\}_{i \in \{0, \dots, N-1\}}$ a set of N shapes associated with a corresponding time point t_i . With analogy to classical random-effect-modelling approaches, we assume that each shape is a random realisation of a common underlying spatiotemporal process $\phi(t)$:

$$S_i = \rho_i(\phi(B_0, t_i)) + \epsilon_i,$$

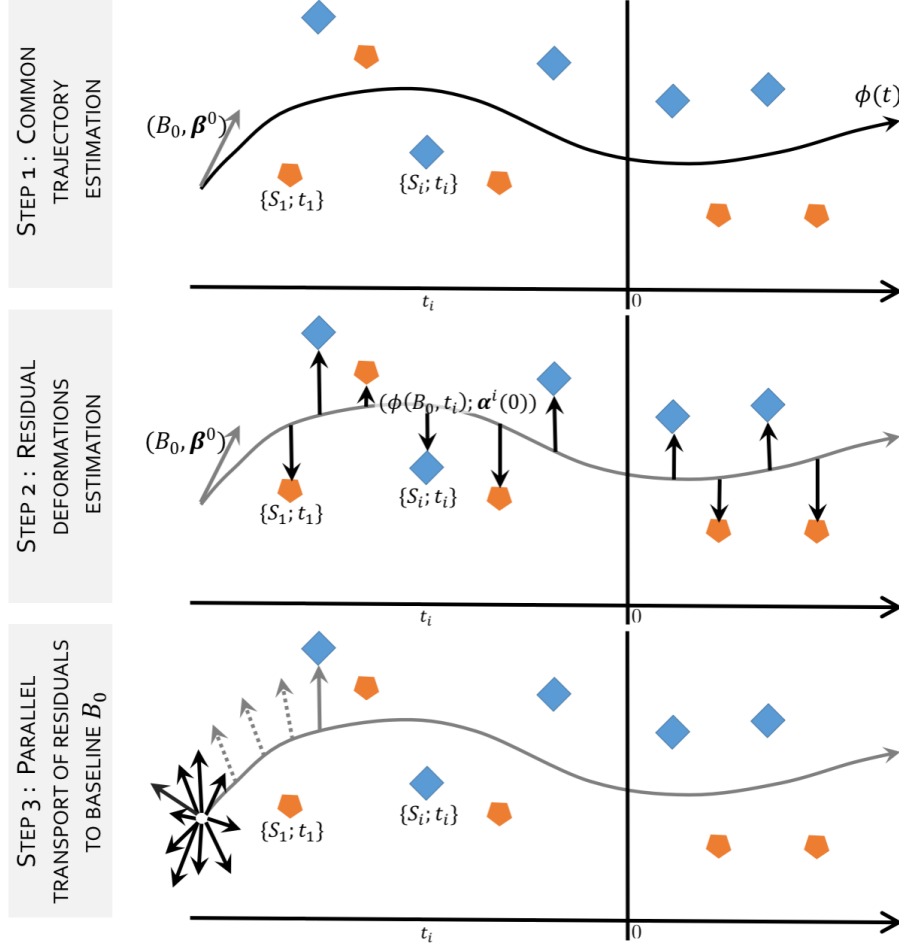
86 where B_0 is a common reference frame, and ρ_i is a subject-specific "residual" deformation
87 accounting for individual deviation from the mean shape. We characterise this
88 residual through the diffeomorphism linking the shape S_i to the corresponding sample of
89 the common spatiotemporal trajectory at time point t_i . We also assume that ϵ_i is Gaussian
90 randomly distributed noise. In order to identify group-wise differences between the
91 given populations, we rely on the analysis of the subjects-specific residuals deformations
92 ρ_i .

93 This is a challenging problem, since all ρ_i are defined at different time points along
94 the common spatiotemporal trajectory, and therefore cannot be directly compared in a
95 common anatomical framework. Moreover, the optimisation of the functional for the
96 simultaneous estimation of the group-wise trajectory and random effects is not trivial,
97 and would ultimately result in expensive and thus impractical numerical schemes. For
98 these reasons, we propose a serial optimisation of the problem by introducing an efficient
99 numerical framework composed of three steps illustrated in Figure 1.

100 (i) First, we assume that the residuals deformations ρ_i are fixed, and we estimate the
101 common trajectory $\phi(t)$. (ii) Second, given the modelled trajectory ϕ , we estimate the
102 residuals deformations ρ_i through non-linear registration between the trajectory point
103 $\phi(B_0, t_i)$ and S_i . (iii) Third, we spatially normalise the residual deformations in the
104 common initial reference space B_0 using parallel transport.

105 The proposed framework relies on the mathematical setting of the Large Diffeomorphic
106 Deformation Metric Mapping (LDDMM) framework and the varifold representation
107 of shapes (section 2.1). This choice allows a mathematically consistent definition of all
108 steps (section 2.2), namely: (i) the spatiotemporal regression, (ii) the ρ_i deformations

Figure 1: Overview of the proposed regression approach. The temporal axis indicates the time variable attached to the data. The residual deformations (step 2) ρ_i parametrised by $(\phi(B_0, t_i); \alpha^i(0))$ computed from the common trajectory (step 1) ϕ parametrised by $(B_0; \beta^0)$, can not be analysed because they are defined on different spaces i.e. $\phi(B_0, t_i)$. They have to be transported to a common space (i.e. B_0) along the geodesic ϕ , so they can be analysed (step 3).



109 estimation, and (iii) the normalisation of the initial momentum of ρ_i through parallel
110 transport.

111 *2.1. Large diffeomorphic deformation metric mapping and varifold representation*

112 The LDDMM framework [14, 15] is a mathematical and algorithmic framework based
113 on flows of diffeomorphisms, which allows comparing anatomical shapes as well as per-
114 forming statistics. The framework used in this paper is a discrete parametrisation of
115 the LDDMM framework, as proposed by Durrleman *et al.* [17], based on a finite set of
116 N_{B_0} control points overlaid on the 3D space enclosing the initial shape B_0 . The control

117 points number and position are independent from the shapes being deformed as they do
 118 not require to be aligned with the shapes' vertices. They are used to define a potentially
 119 infinite-dimensional basis for the parametrization of the deformation. Momentum vec-
 120 tors are associated with the control points and are used as weights for the decomposi-
 121 tion of a given deformations onto this basis.

Deformation maps $\varphi_v : \mathbb{R}^3 \rightarrow \mathbb{R}^3$ are built by integrating time-varying vector fields $(v_t)_{0 \leq t \leq 1}$, such that each $v(\cdot, t)$ belongs to a Reproducing Kernel Hilbert Space (RKHS) V with kernel K_V . We use a Gaussian kernel for all control points x, y :

$$k_V(x, y) = \exp\left(\frac{-|x - y|^2}{\lambda^2}\right) \text{Id},$$

with Id the identity matrix, and λ a scale factor which determines the size of the kernel and therefore the degree of smoothness of the deformations. We define $\varphi_v(x) = \phi_v(x, 1)$ as the diffeomorphism induced by $v(x, t)$ where $\phi_v(x, 1)$ is the unique solution of the differential equation:

$$\frac{d\phi_v}{dt}(x, t) = v(\phi_v(x, t), t), \forall t \in [0, 1] \text{ with } \phi_v(x, 0) = x, \forall x \in \mathbb{R}^3.$$

Velocity fields $v(\cdot, t)$ are controlled via an energy functional $\int_0^1 \|v(\cdot, t)\|_V^2 dt$, where $\|\cdot\|_V$ is a Hilbert norm defined on vector fields of \mathbb{R}^3 , which is used as a regularity term in the matching functional to penalises non-regularity. In the LDDMM framework, matching two shapes S and T requires estimating an optimal deformation map $\phi : \mathbb{R}^3 \rightarrow \mathbb{R}^3$ such that $\phi(S)$ is close to T . This is achieved by optimising

$$d([\varphi_v(S)], [T])^2 + \gamma \int_0^1 \|v(\cdot, t)\|_V^2 dt,$$

122 where γ balances the regularity of ϕ_v against the spatial proximity d , a similarity measure
 123 between the varifold representation of $\varphi_v(S)$ and T noted respectively $[\varphi_v(S)]$ and $[T]$.

In a discrete setting, the vector fields $v(x, t)$ corresponding to optimal maps are expressed as combinations of spline parametrised fields that involve the reproducing kernel K_V of the space V :

$$v(x, t) = \sum_{p=1}^{N_{B_0}} K_V(x, x_p(t)) \alpha_p(t),$$

124 where $x_p(t) = \phi_v(x_p, t)$ are the trajectories of control points x_p . The control points are
 125 regularly spaced on a 3D grid overlaid on the space that contains the mesh of the subject
 126 S . The control point spacing is defined by the size of the kernel K_V . The time-dependent
 127 vectors $\alpha_p(t) \in \mathbb{R}^3$ are referred to as momentum vectors attached to x_p . The full de-
 128 formation can be encoded by the set of initial momentum vectors $\alpha(0) = \{\alpha_p(0)\}_{1 \leq p \leq n}$
 129 located at the points $\{x_p\}_{1 \leq p \leq n}$. This allows to analyse the set of deformation maps
 130 from a given template to the observed shapes by performing statistics on the initial
 131 momentum vectors defined on control points located around the template shape. The
 132 process of generating back any deformation maps from initial conditions $(x_p(0), \alpha_p(0))$,
 133 i.e. integrating the geodesic equations, is called geodesic shooting or exponential map
 134 and is noted $\exp_{x_p(0)}(\alpha_p(0))$.

135 As previously stated, varifolds are used to represent shapes [18]. They are non-
 136 oriented versions of the representation with currents [19], which are used to efficiently
 137 model a large range of shapes. To represent a shape S as a varifold, the shape space is
 138 embedded into the dual space of a Reproducing Kernel Hilbert Space (RKHS) W , noted
 139 W^* , and encoded using a set of non-oriented unit normals attached on each vertices of
 140 the shape. This kernel-based embedding allows to define a distance between different
 141 embedded shapes. Varifolds are robust to varying topologies, do not require point to
 142 point correspondences, and embed the shapes in a vector space, which facilitate the
 143 interpretation of results. The varifold representation of a discretised mesh composed by
 144 M triangles S is noted $[S]$ and writes: $[S](\omega) = \sum_{k=1}^M \omega(c_k) \tau(c_k)^2 / \|\tau(c_k)\|$ with ω a
 145 vector field in W , c_k the centre of the triangle k , and $\tau(c_k)$ the tangent of the surface S
 146 at point c_k .

147 *2.2. Residual extraction framework*

148 Due to the asymmetry of the disease, the proposed framework has been designed so
 149 that it is unbiased to the affected side. For each subject, rather than considering the
 150 left or right structure, we build a mean shape by averaging both sides. First, we flip all
 151 input T1w brain images, in order to have all structures, left and right, on the same side,
 152 right. Second, we affinely align the T1w brain images (the original and the flipped once)
 153 to a subject-specific mid-space [20] before rigidly refining the alignment of the structure
 154 of interest, that has been segmented using the method proposed by Cardoso *et al.* [21].
 155 Third, we extract the meshes of the left (flipped, L_i) and right structures (R_i), and
 156 compute the mean shape, by estimating the diffeomorphisms $\chi_v^{(i)}$ for each subject i , such
 157 as $\chi_v^{(i)} = \operatorname{argmin} \frac{1}{2} (\|[\chi_v^{(i)}(L_i)] - [S_i]\|_{W^*}^2 + \|[\chi_v^{(i)}(R_i)] - [S_i]\|_{W^*}^2) + \gamma \int_0^1 \|v_i(\cdot, t)\|_V^2 dt$ with
 158 S_i the mean shape of subject i and W^* the space of varifolds. The obtained subject-
 159 specific average shape of the structure of interest is noted S_i and is associated with a
 160 temporal information t_i , the number of years to the expected onset (EYO) of the subject
 161 i .

162 The computation of the spatiotemporal regression [12] requires an initial shape $B_0 =$
 163 $\{x_p\}_{p=1, \dots, N_{B_0}}$ as reference. To avoid any bias towards a subject selected as the initial
 164 shape, we estimate the initial shape from the 10 subjects who are the furthest away from
 165 expected symptom onset, so located in time around -40 years before EYO. We estimate
 166 the centroid of those 10 subjects using the diffeomorphic Iterative Centroid method [22],
 167 which estimate a centre of a given population in a reasonable computation time [23].

168 The spatiotemporal regression of the set of shapes $\{(S_i, t_i)\}_{i \in \{0, \dots, N-1\}}$ is imple-
 169 mented in the Deformetrica software [24, 25]². The EYO values are discretised into
 170 T time points. Starting from B_0 at time $t = 0$, a geodesic moving through the positions
 171 $\phi(B_0, t)$, $\forall t \in \{0, \dots, T\}$ is computed by minimising the discrepancy between the model
 172 at time t (i.e. $\phi(B_0, t)$) and the observed shapes S_i :

$$E(\phi_v) = \sum_{t_i} d([\phi_v(B_0, t_i)], [S_i])^2 + \gamma \|v\|_{V^\phi}^2,$$

173 with v the time-varying velocity vector field that belongs to the RKHS V determined
 174 by the Gaussian Kernel K . The initial momentum vectors $\beta^0(0) = \{\beta_p^0(0)\}_{1 \leq p \leq N_{B_0}}$ is

²<http://www.deformetrica.org/>

170 defined on the control point grid overlay on the baseline shape B_0 and fully encodes the
 171 geodesic regression parametrised by $\{B_0; \beta^0(0)\}$.

172 We then compute the residuals diffeomorphic deformations ρ_i between every obser-
 173 vation and the spatio-temporal average shape by estimating a geodesic between $\phi(B_0, t_i)$
 174 and $\{S_i, t_i\}$. This yields a set of trajectories parametrised by $\{\phi(B_0, t_i); \alpha^i(0)\}_{i \in \{0, \dots, N-1\}}$
 175 that encodes the deformations ρ_i from the spatio-temporal regression to all subjects, with
 176 $\alpha^i(0)$ the initial momentum vectors, where the varying parameter is the step of the defor-
 177 mation. This should not be confused with the time we used until now which corresponds
 178 to EYO and time varying deformation of the main spatio-temporal trajectory.

In order to be able to compare this set of momenta, we gather them in the same Euclidean space. This is achieved by transporting all momenta into the initial space of $B_0 = \phi(B_0, 0)$, using a parallel transport method based on Jacobi fields as introduced in [26]. Parallel transporting a vector along a curve (the computed trajectory parametrised by $(B_0; \beta^0(0))$) consists in translating it across the tangent spaces along the curve by preserving its parallelism, according to a given connection. The Levi-Civita connection is used in the LDDMM framework. The vector is parallel transported along the curve if the connection is null for all steps along the curve [27]. We use Jacobi field instead of the Schild's Ladder method [28], to avoid the cumulative errors and the excessive computation time due to the computation of Riemannian Logarithms in the LDDMM framework, required for the Schild's Ladder. The cumulative errors would have differed from subject to subject and thus introduce a bias. Indeed, their distances from the baseline shape vary, as they all are at different points along the temporal axis. The Jacobi field, used to transport a vector $\alpha^i(0)$ from a time t to the time $t_0 = 0$ along the geodesic γ , is defined as:

$$J_{\gamma(t)}(0, -\beta^0(t), \alpha_i(0)) = \frac{\partial}{\partial \epsilon} \exp_{\gamma(t)}(1/T(-\beta^0(t) + \epsilon \alpha_i(0))).$$

179 The transported initial momentum vector $\alpha_i(0)$ is noted $\theta_i(0)$. After parallel transport-
 180 ing all residuals, all initial momentum vectors are defined in B_0 .

181 2.3. Feature extraction for statistical analysis

182 Each transported initial momentum vectors $\theta_i(0)$ is of size $3 \times N_{B_0}$, where N_{B_0} is the
 183 number of control point used to parametrise the geodesics.

184 Jacobian determinants are commonly used to study shrinkage or growth of the surface,
 185 and are a geometric measure derived from the full deformation tensor. In this work we
 186 propose an analysis framework where we decouple the amplitude and the orientation
 187 of the deformation. Such approach still analyse growth and shrinkage, but also other
 188 geometric aspects, such as rotation and torsion, not captured by the surface Jacobian.

189 To analyse direct measures from deformation and to avoid losing statistical power
 190 from doing a large number of comparisons, we propose an original clustering by grouping
 191 the parametrisation $(B_0; \beta^0(0))$ of the spatio-temporal regression ϕ into clusters.

192 To do so, we defined a similarity measure derived from the positions of the
 193 control points x_p , the pairwise angles and the magnitudes of the initial momentum vectors
 194 $\{\beta_p^0(0)\}_{1 \leq p \leq N_{B_0}}$ attached to the control point x_p . The difference between two control
 195 points x_p and $x_q \forall p, q \in \{1, \dots, N_{B_0}\}$ is defined by the euclidean distance, the angle be-
 196 tween two vectors is defined by the cosine. The similarity between p and q is defined

197 by $s(p, q) = -5\|x_p - x_q\|^2 + 2(\cos(\beta_p^0, \beta_q^0) + 1) - \|\beta_p^0\|^2 - \|\beta_q^0\|^2$. Parameters are chosen
198 to balance between vector similarity and control point positions and depend on the dis-
199 tance in mm between two points. The distance is determined by the kernel K_V so that
200 clusters encompass control points and their momentum vectors within the same area and
201 look alike. To estimate those clusters, we used a spectral clustering method [29] using
202 the discretisation approach presented in [30] for initialisation, as it has been shown to
203 be more stable than other approaches such as k-means for initialisation. 3000 different
204 initialisations are generated and we select the best one in term of inertia for spectral
205 clustering. We chose 10 clusters as thought this would be a good balance between re-
206 ducing the number of multiple comparisons while maintaining some spatial specificity in
207 the analyses and equitable clusters. A mean vector is then computed from the parallel
208 transported residuals defined on the control points of the cluster. This is done for each
209 cluster and for each subject. We then obtain N vectors $\{\nu_{i,k}\}$ per cluster k , and 10
210 vectors per subject i .

211 For the statistical analysis, we will use two uncorrelated descriptors for the vectors
212 $\{\nu_{i,k}\}$: the amplitude and the orientation. The orientation of the vectors $\{\nu_{i,k}\}$ is origi-
213 nally represented by 3 angles, one per axis. The angles are then projected via a Principal
214 Component Analysis on the first eigenvector, therefore the orientation of $\{\nu_{i,k}\}$ consid-
215 ered here is represented by one continuous scalar, leading to the set of responsive variable
216 $\{O_{i,k}\}$.

217 3. Data and application

218 As previously mentioned, we applied the proposed framework to the GENFI study
219 and used the thalamus as structure of interest.

220 *Dataset description*

221 All participants included in this study come from the data freeze 1 of the GENFI
222 cohort described in detail in [2]. Initial results from this cohort [2] show volumetric
223 differences in the thalamus at least 5 years before expected age of onset with an effect in
224 all genetic subtypes, and so we chose this well-defined subcortical structure for further
225 analysis. In this paper we used 211 participants, 113 mutation carriers (MAPT=26,
226 GRN=53, C9ORF=34) and 98 non-carriers. All participants have a T1-weighted (T1w)
227 MRI available and an associated expected years to symptom onset (EYO). The EYO is
228 calculated as the difference between the age of the participant at the time of the T1w
229 acquisition and the mean age at onset of affected family members, EYO range from -40
230 years to +20 years. Table 1 shows the demographics of the study participants used in
231 this analysis.

232 *Application to the thalamus*

233 T1w brain images of all subjects were affinely group-wise registered [20], before apply-
234 ing a rigid registration focused solely around the structure of interest. We then extracted
235 the meshes corresponding to the thalamus, including around 2,300 vertices. This resulted
236 in 211 thalamus meshes, representing the mean left and the right shape. Each were asso-
237 ciated with the EYO of the corresponding subject as well as mutation status: non-carrier
238 and mutation carrier (MC). For the spatiotemporal regression, we used 30 time points,

Table 1: Data demographics, in absolute values.

	Non-carriers n=98	Mutation carriers n=113
Males	59	56
Asymptomatic	98	76
Age in years (med (IQR))	50.2 (36.6 - 62.1)	52.7 (41.1 - 62.7)
Years from expected onset:		
≤ -20 years	30	21
$-20 \leq \text{years} \leq -10$	16	21
$-10 \leq \text{years} < 0$	23	22
$0 \leq \text{years}$	29	49

239 which corresponds approximatively to one time point every two years. The space of de-
 240 formations V was defined using a 11mm width kernel, approximately half of the length
 241 of the thalamus, which leads to a set of 288 control points. For the space of varifolds we
 242 used a 5mm width kernel.

243 Similarly to the volumetric analysis performed by Rohrer *et al.* [2], we used a mixed
 244 effect model to study the shape difference between the non-carriers and mutation carriers.
 245 Amplitude $\{|\nu_{i,k}|\}$ and orientation $\{O_{i,k}\}$ were used as responsive variables and the fixed
 246 effects predictors of interest were mutation carrier status, EYO, interaction between
 247 mutation carrier status and EYO, sex and the site in which the subject has been scanned.
 248 A random intercept for family allows values of the marker to be correlated between family
 249 members.

250 We performed a Wald test for every model, assessing the difference between the
 251 mutation carrier group and the non-carrier group, and the evolution of differences across
 252 time. For each analysis with statistically significant differences between both groups,
 253 further Wald tests were conducted every 5 years as in the volumetric analysis [2] to
 254 assess how long before the expected onset we could detect changes between mutation
 255 carriers and controls.

256 4. Results

257 Results for the amplitude and the orientation of the residual momentum vectors
 258 are presented Table 2. We found significant differences, after correction for multiple
 259 comparisons, in cluster 1 and cluster 4, for both tests; T1:differences between MC and
 260 controls and T2: differences over time between MC and controls. Those differences
 261 are significant after Bonferroni correction for multiple comparisons (20 tests). Cluster
 262 1 shows differences in the orientation, and no differences in the amplitude, whereas
 263 cluster 4 shows significant differences for those 2 tests in amplitude, and no differences
 264 in orientation. Those 2 clusters are thus selected for the next wald test step. Wald
 265 tests were conducted every 5 years between 20 years before the expected onset and
 266 10 years after the expected onset to limit the number of tests, since we don't expect
 267 changes before -20 EYO, and results are shown in Figure 2, the p-values and confidence
 268 intervals are corrected for multiple comparison across time using Bonferroni correction.

Table 2: p-values with the corresponding χ^2 value, resulting from the Wald tests testing the mutation carrier (MC) differences (test T1), and the evolution of those differences along time (test T2), for the amplitude of the initial momentum vector and its orientation, for the clusters showing at least one significant test. Bold p-values: ≤ 0.05 , and starred (*) p-values indicate the corrected threshold for multiple comparisons: $\leq 2.5e-3$.

		C1	C2	C4	C6	C7
Ampl.	T1	$p = 0.48$ $\chi^2_{df=2} = 1.43$	$p = 0.51$ $\chi^2_{df=2} = 1.35$	$p = \mathbf{1.5e-3} (*)$ $\chi^2_{df=2} = 12.94$	$p = 0.08$ $\chi^2_{df=2} = 5.10$	$p = 0.76$ $\chi^2_{df=2} = 0.55$
	T2	$p = 0.24$ $\chi^2_{df=1} = 1.37$	$p = 0.26$ $\chi^2_{df=1} = 1.28$	$p = \mathbf{1.5e-3} (*)$ $\chi^2_{df=1} = 10.08$	$p = \mathbf{0.04}$ $\chi^2_{df=1} = 4.20$	$p = 0.68$ $\chi^2_{df=1} = 0.17$
Orient.	T1	$p = \mathbf{2e-4} (*)$ $\chi^2_{df=2} = 16.60$	$p = 0.12$ $\chi^2_{df=2} = 4.17$	$p = 0.85$ $\chi^2_{df=2} = 0.33$	$p = 0.63$ $\chi^2_{df=2} = 0.92$	$p = 0.08$ $\chi^2_{df=2} = 5.06$
	T2	$p = \mathbf{9e-4} (*)$ $\chi^2_{df=1} = 11.01$	$p = \mathbf{0.05}$ $\chi^2_{df=1} = 3.85$	$p = 0.62$ $\chi^2_{df=1} = 0.25$	$p = 0.34$ $\chi^2_{df=1} = 0.91$	$p = \mathbf{0.04}$ $\chi^2_{df=1} = 4.29$

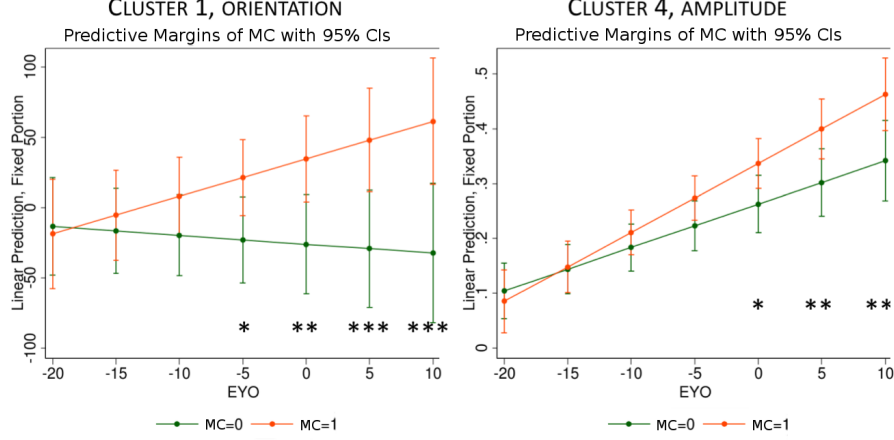
269 The orientation of the cluster 1 deformation shows significant differences between the
 270 mutation carriers and controls, 5 years before EYO ($p = 0.03$), the uncorrected for this
 271 cluster is $p = 2e-3$, to keep a head to head comparison with the previous studies on
 272 this dataset [2, 13] in which the p-values at -5 EYO was significant but higher than
 273 here. The uncorrected p-values show significant differences at 10 years before EYO,
 274 with $p=0.048$ for the orientation of cluster 1. The amplitude between the two groups
 275 doesn't differ significantly for the cluster 4 before EYO for corrected p-values, and differs
 276 5 years before onset without correction ($p=0.05$). Figure 3 shows the initial momentum
 277 vectors of clusters 1 and 4, and the amount of displacement due to the deformations
 278 corresponding to those clusters 1 and 4, where each cluster has its own colour scale, since
 279 the maximum displacement for cluster 4 is about 3 mm, against 9 mm for cluster 1.
 280 Deformations affect more the anterior part of the thalamus.

281 Since the number of clusters used (10), is an arbitrary choice, we tried to reproduce the
 282 results with different number of clusters. We performed the analysis for 2, 4, 6, 8, 10, 12,
 283 14 and 16 clusters. For 6 clusters and 16 clusters, there were differences in orientation for
 284 one of the clusters which deformation corresponds to the one of cluster 1 (see Figure 3).
 285 From 8 clusters to 14 clusters, we found a cluster with strong differences 5 years before
 286 the expected onset ($p < 0.01$) in orientation whose deformation corresponds again to
 287 the one of the cluster 1 ($p = 0.003$). The change in orientation for the deformation
 288 recovered within cluster 1 (see Figure 3) appears to be stable for different clusterings
 289 of the deformation parametrisation of the global spatiotemporal trajectory. All results
 290 regarding the different number of clusters can be found in supplementary material (doi.
 291 org/10.5281/zenodo.1324234).

292 5. Discussion and conclusion

293 We applied a novel method of statistical shape analysis to a cohort of individuals with
 294 genetic FTD in order to localise any presymptomatic differences present in the shape of
 295 the thalamus. From the analysis, we conclude that differences are observed five years

Figure 2: cluster 1 (orientation component) and cluster 4 (amplitude component) estimates in mutation carriers and controls, by estimated time from expected symptoms onset (EYO). p-values and confident interval are Bonferroni corrected. * : $p < 0.05$, ** : $p < 0.01$, *** : $p < 0.001$

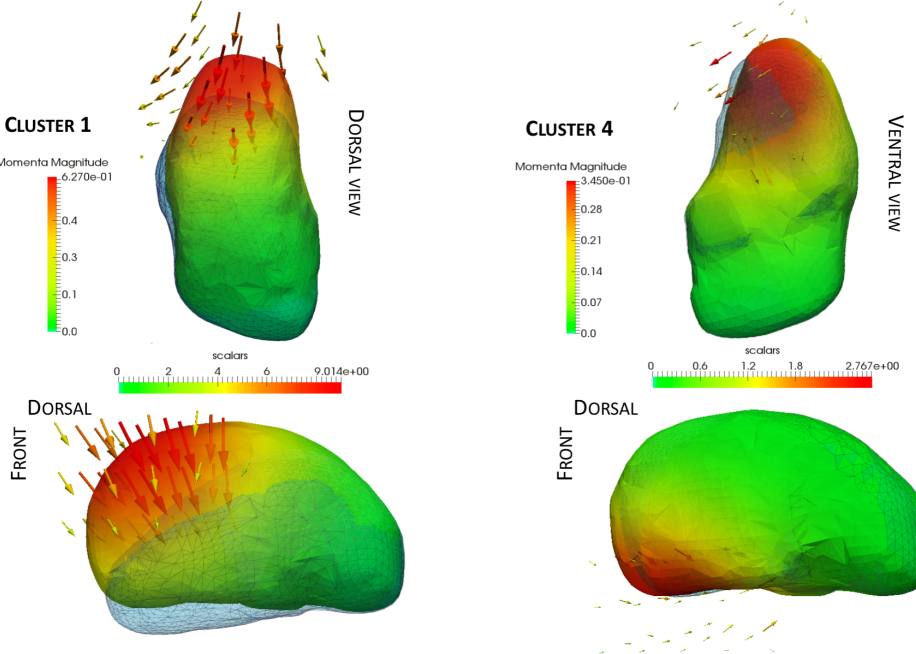


296 before expected symptom onset. While volumetric analysis [2] and our initial shape
 297 analysis [13] also found these changes, this method showed significance that survived
 298 correction for multiple comparisons. The change in shape is primarily attributable to
 299 differences in orientation of the deformation rather than changes in amplitude of the
 300 deformation, which would imply a simple scaling effect of the region. This result con-
 301 firms our previous shape analysis in this cohort [13] that was performed at a global
 302 level through a kernel principal component analysis. The first mode of variation which
 303 detected significant shape differences around the same point with respect to EYO did
 304 not capture volume differences but only changes in the orientation of the deformation.
 305 The results of those studies seem to indicate that shape changes occur before volume
 306 changes. As many regions of the thalamus contain a mixture of grey and white matter,
 307 these shape changes may reflect subtle shifts in the ratio between these two tissue types
 308 in the areas affected.

309 The regions of the thalamus most affected in the analysis are anterior, overlapping
 310 with the anterior nuclei group. The main connections of these nuclei are to the pre-
 311 frontal cortices, an area universally affected in all genetic forms of FTD. To illustrate
 312 this purpose, we used the Oxford thalamic connectivity atlas, a thalamic atlas based on
 313 its anatomical connectivity to the cerebral cortex [31], and displayed at Figure 4 the atlas
 314 next to the clusters 1 and 4. Whilst differences are seen in cortical involvement within
 315 the different genetic forms of FTD [32], it may well be that this joint analysis of GRN,
 316 C9orf72 and MAPT mutations is only identifying thalamic regions jointly affected.

317 Another interesting cortical region involved in FTD, could also be analysed with this
 318 method: the insula, which is located in the lateral sulci and is connected to the limbic
 319 system, and to the thalamus. It would be interesting to analyse the insula and thalamus
 320 together, and the insula only, so we could investigate if shape changes in both structures
 321 are linked.

Figure 3: Deformation obtained by the momentum vectors (displayed here and coloured by amplitude) of Cluster 1 and Cluster 4. The colour map is in millimetres and indicates the displacement due to the corresponding deformation (blue meshes). The scale for Cluster 1 range from 0 mm to 9 mm, and from 0 mm to 2.8 mm for Cluster 4.



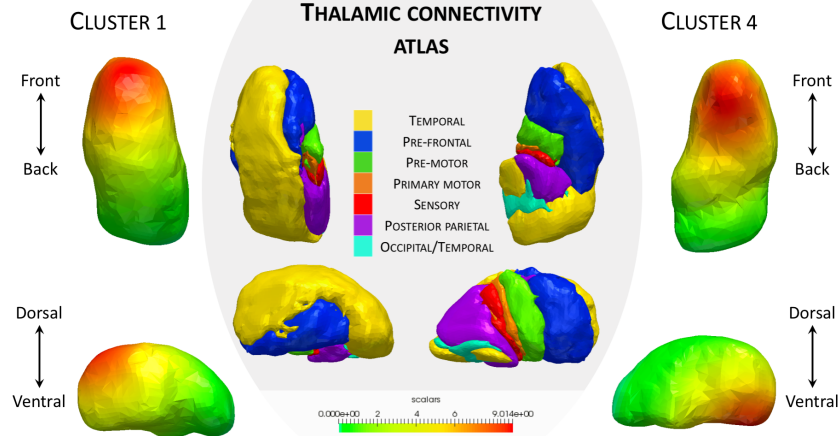
322 The small numbers in each group precluded any analysis of the individual genetic
 323 types, but it will be important to investigate future data freezes from the GENFI study
 324 with larger numbers, particularly the C9orf72 group who have been shown to have early
 325 thalamic involvement [32].

326 Future studies should also evaluate the initial momentum vectors of individual geodesic
 327 evolution of shapes from each subject, through longitudinal data. Those individual evo-
 328 lutions will provide information on the differences of evolutions of shape between the
 329 mutation carriers and the controls.

330 **Acknowledgements**

331 Claire Cury is supported by the EU-FP7 project VPH-DARE@IT (FP7-ICT-2011-
 332 9-601055). Stanley Durrleman has received funding from the program Investissements
 333 davenir ANR-10-IAIHU-06 and the European Unions Horizon 2020 research and inno-
 334 vation programme EuroPOND under grant agreement No 666992, and is funded by the
 335 European Research Council (ERC) under grant agreement No 678304. Marco Lorenzi re-
 336 ceived funding from the EPSRC (EP/J020990/1). Jennifer Nicholas is supported by UK
 337 Medical Research Council (grant MR/M023664/1). David Cash is supported by grants
 338 from the Alzheimer Society(AS-PG-15-025), Alzheimers Research UK (ARUK-PG2014-
 339 1946) and Medical Research Council UK (MR/M023664/1). JBR is supported by the

Figure 4: Thalamic connectivity atlas, and deformations clusters 1 and 4. The orientation of cluster 1 leads to significant differences between MC and controls 5 years before EYO.



340 Wellcome Trust (103838). Jonathan D. Rohrer is an MRC Clinician Scientist and has
341 received funding from the NIHR Rare Diseases Translational Research Collaboration. Se-
342 bastien Ourselin receives funding from the EPSRC (EP/H046410/1, EP/K005278), the
343 MRC (MR/J01107X/1), the NIHR Biomedical Research Unit (Dementia) at UCL and the
344 National Institute for Health Research University College London Hospitals Biomedical
345 Research Centre (NIHR BRC UCLH/UCL High Impact Initiative- BW.mn.BRC10269).
346 Marc Modat is supported by the UCL Leonard Wolfson Experimental Neurology Centre
347 (PR/ylr/18575) and Alzheimers Society UK (AS-PG-15-025). We would like to thank
348 the participants and their families for taking part in the GENFI study.

349 References

350 [1] J. D. Rohrer, J. D. Warren, Phenotypic signatures of genetic frontotemporal dementia:, Current
351 Opinion in Neurology 24 (6) (2011) 542–549. doi:[10.1097/WCO.0b013e32834cd442](https://doi.org/10.1097/WCO.0b013e32834cd442).

352 [2] J. D. Rohrer, J. M. Nicholas, D. M. Cash, J. van Swieten, E. Doppler, L. Jiskoot, R. van Minkelen,
353 S. A. Rombouts, M. J. Cardoso, S. Clegg, M. Espak, S. Mead, D. L. Thomas, E. D. Vita, et al.,
354 Presymptomatic cognitive and neuroanatomical changes in genetic frontotemporal dementia in the
355 Genetic Frontotemporal dementia Initiative(GENFI) study: a cross-sectional analysis, The Lancet
356 Neurology 14 (3) (2015) 253–262. doi:[10.1016/S1474-4422\(14\)70324-2](https://doi.org/10.1016/S1474-4422(14)70324-2).

357 [3] M. Bocchetta, E. Gordon, M. J. Cardoso, M. Modat, S. Ourselin, J. D. Warren, J. D. Rohrer,
358 Thalamic atrophy in frontotemporal dementia - Not just a C9orf72 problem, NeuroImage: Clinical.
359 [4] M. Boccardi, L. Bresciani, C. Geroldi, A. Beltramello, G. B. Frisoni, M. P. Laakso, Clinical char-
360 acteristics of frontotemporal patients with symmetric brain atrophy, European Archives of Psychiatry
361 and Clinical Neuroscience 252 (5) (2002) 235–239. doi:[10.1007/s00406-002-0388-z](https://doi.org/10.1007/s00406-002-0388-z).

362 [5] T. L. S. Benzinger, T. Blazey, C. R. Jack, et al., Regional variability of imaging biomarkers in
363 autosomal dominant Alzheimer's disease., Proceedings of the National Academy of Sciences 110 (47)
364 (2013) E4502–9.

365 [6] J. M. Schott, J. W. Bartlett, N. C. Fox, J. Barnes, Increased brain atrophy rates in cognitively
366 normal older adults with low cerebrospinal fluid A β 1-42., Annals of neurology 68 (6) (2010) 825–
367 34. doi:[10.1002/ana.22315](https://doi.org/10.1002/ana.22315).
368 URL <http://www.ncbi.nlm.nih.gov/pubmed/21181717>

369 [7] M. Lorenzi, N. Ayache, G. Frisoni, X. Pennec, et al., 4D registration of serial brain's MR images: a
370 robust measure of changes applied to Alzheimer's disease, in: MICCAI Workshop, Spatio Temporal
371 Image Analysis Workshop (STIA), 2010.

372 [8] M. Lorenzi, X. Pennec, G. B. Frisoni, N. Ayache, Disentangling normal aging from Alzheimer's
373 disease in structural magnetic resonance images, *Neurobiology of Aging* 36 (2015) S42–S52. doi:
374 [10.1016/j.neurobiolaging.2014.07.046](https://doi.org/10.1016/j.neurobiolaging.2014.07.046).

375 [9] M. Datar, P. Muralidharan, A. Kumar, S. Gouttard, J. Piven, G. Gerig, R. Whitaker, P. T. Fletcher,
376 Mixed-Effects Shape Models for Estimating Longitudinal Changes in Anatomy, in: D. Hutchi-
377 son, T. Kanade, J. Kittler, J. M. Kleinberg, F. Mattern, J. C. Mitchell, M. Naor, O. Nierstrasz,
378 C. Pandu Rangan, B. Steffen, M. Sudan, D. Terzopoulos, D. Tygar, M. Y. Vardi, G. Weikum,
379 S. Durrleman, T. Fletcher, G. Gerig, M. Niethammer (Eds.), *Spatio-temporal Image Analysis for*
380 *Longitudinal and Time-Series Image Data*, Vol. 7570, Springer Berlin Heidelberg, Berlin, Heidel-
381 *berg*, 2012, pp. 76–87.

382 [10] P. Muralidharan, J. Fishbaugh, H. J. Johnson, S. Durrleman, J. S. Paulsen, G. Gerig, P. T.
383 Fletcher, Diffeomorphic Shape Trajectories for Improved Longitudinal Segmentation and Statistics,
384 in: P. Golland, N. Hata, C. Barillot, J. Hornegger, R. Howe (Eds.), *Medical Image Computing and*
385 *Computer-Assisted Intervention ??? MICCAI 2014*, Vol. 8675, Springer International Publishing,
386 2014, pp. 49–56.

387 [11] L. Younes, M. Albert, M. I. Miller, B. R. Team, et al., Inferring changepoint times of medial temporal
388 lobe morphometric change in preclinical alzheimer's disease, *NeuroImage: Clinical* 5 (2014) 178–187.

389 [12] S. Durrleman, X. Pennec, A. Trouvé, J. Braga, G. Gerig, N. Ayache, Toward a comprehensive
390 framework for the spatiotemporal statistical analysis of longitudinal shape data, *International*
391 *Journal of Computer Vision* 103 (1) (2013) 22–59. doi:[10.1007/s11263-012-0592-x](https://doi.org/10.1007/s11263-012-0592-x).

392 [13] C. Cury, M. Lorenzi, D. Cash, J. M. Nicholas, A. Routier, J. Rohrer, S. Ourselin, S. Durrleman,
393 M. Modat, Spatio-Temporal Shape Analysis of Cross-Sectional Data for Detection of Early Changes
394 in Neurodegenerative Disease, in: M. Reuter, C. Wachinger, H. Lombaert (Eds.), *Spectral and*
395 *Shape Analysis in Medical Imaging*, Vol. 10126, Springer International Publishing, 2016, pp. 63–75.
396 doi:[10.1007/978-3-319-51237-2\6](https://doi.org/10.1007/978-3-319-51237-2\6).

397 URL http://link.springer.com/10.1007/978-3-319-51237-2_6

398 [14] A. Trouvé, Diffeomorphisms groups and pattern matching in image analysis, *International Journal*
399 *of Computer Vision* 28 (3) (1998) 213–221.

400 [15] M. F. Beg, M. I. Miller, A. Trouvé, L. Younes, Computing large deformation metric mappings via
401 geodesic flows of diffeomorphisms, *International Journal of Computer Vision* 61 (2) (2005) 139–157.

402 [16] J. Glaunès, A. Qiu, M. I. Miller, L. Younes, Large Deformation Diffeomorphic Metric Curve Map-
403 ping, *International Journal of Computer Vision* 80 (3) (2008) 317–336.

404 [17] S. Durrleman, M. Prastawa, G. Gerig, S. Joshi, Optimal Data-Driven Sparse Parameterization of
405 Diffeomorphisms for Population Analysis, in: D. Hutchison, T. Kanade, J. Kittler, J. M. Kleinberg,
406 F. Mattern, J. C. Mitchell, M. Naor, O. Nierstrasz, C. Pandu Rangan, B. Steffen, M. Sudan,
407 D. Terzopoulos, D. Tygar, M. Y. Vardi, G. Weikum, G. Sz?kely, H. K. Hahn (Eds.), *Information*
408 *Processing in Medical Imaging*, Vol. 6801, Springer Berlin Heidelberg, Berlin, Heidelberg, 2011, pp.
409 123–134.

410 [18] N. Charon, A. Trouvé, The Varifold Representation of Nonoriented Shapes for Diffeomorphic Reg-
411 istration, *SIAM Journal on Imaging Sciences* 6 (4) (2013) 2547–2580. doi:[10.1137/130918885](https://doi.org/10.1137/130918885).

412 [19] M. Vaillant, J. Glaunès, Surface matching via currents, in: G. E. Christensen, M. Sonka (Eds.), *In-*
413 *formation Processing in Medical Imaging*, Vol. 3565 of *Lecture Notes in Computer Science*, Springer
414 Berlin Heidelberg, 2005, pp. 381–392.

415 [20] M. Modat, D. M. Cash, P. Daga, G. P. Winston, J. S. Duncan, S. Ourselin, Global image registration
416 using a symmetric block-matching approach, *Journal of Medical Imaging* 1 (2) (2014) 024003–
417 024003.

418 [21] M. J. Cardoso, K. Leung, M. Modat, S. Keihanejad, D. Cash, J. Barnes, N. C. Fox, S. Ourselin, for
419 ADNI, STEPS: Similarity and truth estimation for propagated segmentations and its application to
420 hippocampal segmentation and brain parcelation., *Medical Image Analysis* 17 (6) (2013) 671–684.

421 [22] C. Cury, J. A. Glaunès, O. Colliot, Diffeomorphic iterative centroid methods for template esti-
422 mation on large datasets, in: F. Nielsen (Ed.), *Geometric Theory of Information, Signals and*
423 *Communication Technology*, Springer International Publishing, 2014, pp. 273–299.

424 [23] C. Cury, J. A. Glaunes, R. Toro, M. Chupin, G. Shumann, V. Frouin, J. b. Poline, O. Colliot,
425 T. I. c, , Statistical shape analysis of large datasets based on diffeomorphic iterative centroids,
426 preprint on webpage at <https://www.biorxiv.org/content/early/2018/07/06/363861>. Submitted
427 to *Frontiers in Neuroscience* (2018). arXiv:<https://www.biorxiv.org/content/early/2018/07/06/363861>

428 06/363861.full.pdf, doi:10.1101/363861.

429 [24] S. Durrleman, M. Prastawa, N. Charon, J. R. Korenberg, S. Joshi, G. Gerig, A. Trouvé, Morphometry of anatomical shape complexes with dense deformations and sparse parameters, *NeuroImage* 101 (0) (2014) 35 – 49. doi:<http://dx.doi.org/10.1016/j.neuroimage.2014.06.043>.

430 [25] A. Routier, P. Gori, A. B. G. Fouquier, S. Lecomte, O. Colliot, S. Durrleman, Evaluation of morphometric descriptors of deep brain structures for the automatic classification of patients with Alzheimer's disease, mild cognitive impairment and elderly controls, in: *MICCAI Workshop, Challenge on Computer-Aided Diagnosis of Dementia Based on Structural MRI Data*, 2014.

431 [26] L. Younes, Jacobi fields in groups of diffeomorphisms and applications, *Quarterly of applied mathematics* 65 (2007) 113–134.

432 [27] M. Lorenzi, X. Pennec, Efficient Parallel Transport of Deformations in Time Series of Images: From Schild???s to Pole Ladder, *Journal of Mathematical Imaging and Vision* 50 (1-2) (2013) 5–17.

433 [28] A. Kheyfets, W. A. Miller, G. A. Newton, Schild's Ladder Parallel Transport Procedure for an Arbitrary Connection, *International Journal of Theoretical Physics* 39 (12) (2000) 2891–2898. doi:10.1023/A:1026473418439.

434 [29] U. von Luxburg, A Tutorial on Spectral Clustering (Nov. 2007).

435 [30] S. Y. Jianbo, S. X. Yu, J. Shi, Multiclass Spectral Clustering, in: *In International Conference on Computer Vision*, 2003, pp. 313–319.

436 [31] T. E. J. Behrens, H. Johansen-Berg, M. W. Woolrich, S. M. Smith, C. a. M. Wheeler-Kingshott, P. A. Boulby, G. J. Barker, E. L. Sillery, K. Sheehan, O. Ciccarelli, A. J. Thompson, J. M. Brady, P. M. Matthews, Non-invasive mapping of connections between human thalamus and cortex using diffusion imaging, *Nature Neuroscience* 6 (7) (2003) 750–757. doi:10.1038/nn1075.

437 [32] D. M. Cash, M. Bocchetta, D. L. Thomas, K. M. Dick, J. C. van Swieten, B. Borroni, D. Galimberti, M. Masellis, M. C. Tartaglia, J. B. Rowe, C. Graff, F. Tagliavini, G. B. Frisoni, J. Laforce, Robert, E. Finger, A. de Mendon?a, S. Sorbi, M. N. Rossor, S. Ourselin, J. D. Rohrer, Patterns of gray matter atrophy in genetic frontotemporal dementia: results from the GENFI study, *Neurobiology of Aging* 62 (2018) 191 – 196.

438

439

440

441

442

443

444

445

446

447

448

449

450

451

452

453

454

455 List of other GENFI consortium members

456 Christin Andersson - Department of Clinical Neuroscience, Karolinska Institutet, Stockholm, Sweden

457

458 Silvana Archetti - Biotechnology Laboratory, Department of Diagnostics, Civic Hospital of Brescia, Brescia, Italy

459

460 Andrea Arighi - Neurology Unit, Department of Physiopathology and Transplantation, Fondazione C Granda, Istituto di Ricovero e Cura a Carattere Scientifico Ospedale Policlinico, Milan, Italy

461

462 Luisa Benussi - Istituto di Ricovero e Cura a Carattere Scientifico Istituto Centro San Giovanni di Dio Fatebenefratelli, Brescia, Italy

463

464 Sandra Black - LC Campbell Cognitive Neurology Research Unit, Sunnybrook Research Institute, Toronto, Canada

465

466 Maura Cosseddu - Centre of Brain Aging, University of Brescia, Brescia, Italy

467

468 Marie Fallström - Department of Geriatric Medicine, Karolinska University Hospital, Stockholm, Sweden

469

470 Carlos Ferreira - Instituto Cincias Nucleares Aplicadas Sade, Universidade de Coimbra, Coimbra, Portugal

471

472 Chiara Fenoglio - Dept. of Pathophysiology and Transplantation, "Dino Ferrari" Center, University of Milan, Fondazione C Granda, IRCCS Ospedale Maggiore Policlinico, Milan, Italy

473

474 Nick Fox - Dementia Research Centre, UCL Institute of Neurology, London, UK

475

476 Morris Freedman - Division of Neurology, Baycrest Centre for Geriatric Care, University of Toronto, Canada

477

478 Giorgio Fumagalli - Neurology Unit, Fondazione C Granda, Istituto di Ricovero e
479 Cura a Carattere Scientifico Ospedale Policlinico, Milan, Italy
480 Stefano Gazzina - Centre of Brain Aging, Neurology Unit, Department of Clinical
481 and Experimental Sciences, University of Brescia, Brescia, Italy
482 Roberta Ghidoni - Istituto di Ricovero e Cura a Carattere Scientifico Istituto Centro
483 San Giovanni di Dio Fatebenefratelli, Brescia, Italy
484 Marina Grisoli - Fondazione Istituto di Ricovero e Cura a Carattere Scientifico Istituto
485 Neurologico Carlo Besta, Milano, Italy
486 Vesna Jelic - Division of Clinical Geriatrics, Karolinska Institutet, Stockholm, Sweden
487 Lize Jiskoot - Department of Neurology, Erasmus Medical Center, Rotterdam, The
488 Netherland
489 Ron Keren - University Health Network Memory Clinic, Toronto Western Hospital,
490 Toronto, Canada
491 Gemma Lombardi - Department of Neuroscience, Psychology, Drug Research and
492 Child Health, University of Florence, Florence, Italy
493 Carolina Maruta - Lisbon Faculty of Medicine, Language Research Laboratory, Lis-
494 bon, Portugal
495 Lieke Meeter - Department of Neurology, Erasmus Medical Center, Rotterdam, The
496 Netherlands
497 Rick van Minkelen - Department of Clinical Genetics, Erasmus Medical Center, Rot-
498 terdam, The Netherland
499 Benedetta Nacmias - Department of Neuroscience, Psychology, Drug Research and
500 Child Health, University of Florence, Florence, Italy
501 Linn ijerstedt - Division of Neurogeriatrics, Karolinska Institutet, Stockholm, Sweden
502 Alessandro Padovani - Neurology Unit, Department of Medical and Experimental
503 Sciences, University of Brescia, Brescia, Italy
504 Jessica Panman - Department of Neurology, Erasmus Medical Center, Rotterdam,
505 The Netherland
506 Michela Pievani - Istituto di Ricovero e Cura a Carattere Scientifico Istituto Centro
507 San Giovanni di Dio Fatebenefratelli, Brescia, Italy
508 Cristina Polito - Department of Clinical Pathophysiology, University of Florence,
509 Florence, Italy
510 Enrico Premi - Centre for Ageing Brain and Neurodegenerative Disorders, Neurology
511 Unit, University of Brescia, Brescia, Italy
512 Sara Prioni - Fondazione Istituto di Ricovero e Cura a Carattere Scientifico Istituto
513 Neurologico Carlo Besta, Milano, Italy
514 Rosa Rademakers - Department of Neurosciences, Mayo Clinic, Jacksonville, Florida
515 Veronica Redaelli - Fondazione Istituto di Ricovero e Cura a Carattere Scientifico
516 Istituto Neurologico Carlo Besta, Milano, Italy
517 Ekaterina Rogaeva - Tanz Centre for Research in Neurodegenerative Diseases, Uni-
518 versity of Toronto, Canada
519 Giacomina Rossi - Fondazione Istituto di Ricovero e Cura a Carattere Scientifico
520 Istituto Neurologico Carlo Besta, Milano, Italy
521 Martin Rossor - Dementia Research Centre, UCL Institute of Neurology, London, UK
522 Elio Scarpini - Neurology Unit, Department of Physiopathology and Transplanta-
523 tion, Fondazione C Granda, Istituto di Ricovero e Cura a Carattere Scientifico Ospedale
524 Policlinico, Milan, Italy

525 David Tang-Wai - University Health Network Memory Clinic, Toronto Western Hos-
526 pital, Toronto, Canada
527 Carmela Tartaglia - Tanz Centre for Research in Neurodegenerative Diseases, Uni-
528 versity of Toronto, Canada
529 Hakan Thonberg - Center for Alzheimer Research, Division of Neurogeriatrics, Karolin-
530 ska Institutet, Stockholm, Sweden
531 Pietro Tiraboschi - Fondazione Istituto di Ricovero e Cura a Carattere Scientifico
532 Istituto Neurologico Carlo Besta, Milano, Italy
533 Ana Verdelho - Department of Neurosciences, Santa Maria Hospital, University of
534 Lisbon, Portugal
535 Jason Warren - Dementia Research Centre, UCL Institute of Neurology, London, UK